

Evaluation of performance and acoustic signature of flexible marine propellers under consideration of fluid-structure interaction by means of partitioned simulation

Tobias Lampe¹, Lars Radtke², Ulf Göttsche¹, Alexander Düster², Moustafa Abdel-Maksoud¹

¹ Institute for Fluid Dynamics and Ship Theory (FDS), Hamburg University of Technology, Germany

² Institute for Ship Structural Design and Analysis (SKF), Hamburg University of Technology, Germany

ABSTRACT

The present article deals with the evaluation of performance and acoustic signature of cavitating flexible marine propellers in stationary as well as instationary inflow conditions. A partitioned solution approach is utilized here to solve the coupled fluid-structure interaction problem. For the fluid domain, a potential theory based boundary element method is used while the structural domain is covered by a high-order FEM. Information exchange between both sub-problems is managed by a C++ based environment for the general solution of multi-field problems. The acoustic evaluation is performed in a post-processing fashion utilizing the Ffowcs-Williams Hawkins equation. Different setups including a propeller, cavitation effects and blade flexibility are investigated with regard to performance and acoustic signature.

Keywords

propeller, fluid-structure-interaction, quasi-newton least-squares algorithm, fflowcs williams-hawkings equation

1 INTRODUCTION

The structural-dynamic behaviour of marine propellers, as well as the corresponding effects on performance, induced vibrations as well as the acoustic signature, is usually taken into account in a severely simplified manner or completely omitted in conventional propeller design procedures. With regard to modern propellers, which, for instance, include designs with high blade skew or make use of novel materials, blade vibrations and deformations can not be ignored and have therefore gained increasing importance. It is therefore desirable to develop simulation techniques which are capable of handling the complex interaction of all involved domains.

In this work, this task is taken care of by the use of a partitioned solution approach. For both, structural and fluid domain, sophisticated simulation methods and the corresponding discretizations are employed. Information transfer at the domain interface is handled by *comana* (König et al., 2016), which is also responsible for the acceleration of the solution process by means of the Quasi-Newton

Least-Squares algorithm. The hydrodynamic part of the simulations is calculated by means of the potential theory based software *panMARE* (Berger et al., 2014), while the structural simulation is performed with *AdhoC* (Düster et al., 2001). All of the utilized software is developed at the FDS and SKF institutes. In order to obtain an acoustic evaluation of the far field while taking into account the compressibility of the fluid, the Ffowcs-Williams Hawkins Equation (FWHE) in Formulation 1A by Brentner and Farassat (2003) is utilized.

The capabilities of the approach are demonstrated based on the well known P1356 propeller of the KCS container ship, which is investigated with regard to the influence of propeller blade flexibility on performance and acoustic signature. Since no validation data regarding the influence of fluid-structure interaction (FSI) effects on the acoustical properties of marine propellers is available, the paper's main intention is to highlight the capabilities of the proposed simulation approach.

2 SIMULATION METHOD

2.1 Fluid Domain

For the calculation of the fluid domain, *panMARE* is employed. Following a potential theory based approach, the flow is assumed as irrotational, incompressible and inviscid, yielding the Laplace equation

$$\nabla^2\Phi = \frac{\partial^2\Phi}{\partial x^2} + \frac{\partial^2\Phi}{\partial y^2} + \frac{\partial^2\Phi}{\partial z^2} = 0 \quad (1)$$

and the unsteady Bernoulli equation

$$p = p_\infty + \frac{\rho}{2}(\nabla\Phi)^2 - \rho\frac{\partial\phi}{\partial t} + \rho gh \quad (2)$$

as the governing equations. In this context x, y, z refer to a point of interest, p to pressure, p_∞ to reference pressure, ρ to fluid density, t to time, g to the gravitational constant and h to the hydrostatic height, respectively. The velocity potential Φ is taken as a linear combination of the body's boundary speed potential relative to the fixed frame coordinate system Φ_{move} as well the potential contributions due to background flow Φ_{ext} and induced influence of the body

boundaries Φ_{ind} :

$$\Phi = \Phi_{ind} + \Phi_{ext} + \Phi_{move}. \quad (3)$$

In this context, Φ_{move} and Φ_{ext} are given according to the respective simulation setup. Utilizing Green's Identity and the definitions of sources σ and doublets μ

$$-\sigma = \frac{\partial \Phi}{\partial n} - \frac{\partial \Phi_I}{\partial n}, \quad (4)$$

$$-\mu = \Phi - \Phi_I, \quad (5)$$

with Φ_I as the potential inside the body boundaries, a general solution for Equation (1) is obtained. The terms $\frac{\partial \Phi}{\partial n}$ and $\frac{\partial \Phi_I}{\partial n}$ imply the gradient of velocity potential and inner potential in direction of the surface normal vector. Introducing the distinction between body surface S_B and wake surface S_W yields

$$\Phi_{ind} = \frac{1}{4\pi} \left[\int_{S_B} \mu \frac{\partial}{\partial n} \frac{1}{r} - \sigma \frac{1}{r} dS + \int_{S_W} \mu \frac{\partial}{\partial n} \frac{1}{r} dS \right]. \quad (6)$$

The equation system arising from a discrete version of Equation (6) can be solved after applying the Kutta condition (Neitzel et al., 2015) to obtain the doublet strength in the shed wake and specifying the source strength on body panels according to

$$\sigma = \mathbf{n}_P \cdot \mathbf{v}_T, \quad (7)$$

with \mathbf{n}_P as the panel normal vector and \mathbf{v}_T as the total velocity including rigid body movement as well as velocity components due to FSI effects.

2.1.1 Cavitation

In this work, a partially non-linear model is applied to calculate the cavity thickness. Two additional boundary conditions, *dynamic* and *kinematic*, are considered. An initial guess for the cavity extent is given by the local pressure coefficient $C_{p,v}$ and the cavitation number σ_v , yielding the condition

$$C_{p,v} + \sigma_v \leq 0. \quad (8)$$

A converged solution for the cavitating body is obtained in an iterative process. The dipole strength on the cavitating part of the body is specified according to the dynamic boundary condition. Then, in a manner similar to Equation (6), an equation system with cavitating panels is set up and solved to obtain a new flow field. The cavity thickness is calculated according to the kinematic boundary condition and the boundaries of the cavity are moved if the thicknesses at the cavity closure exceed a threshold. If the boundaries have been moved, the dynamic boundary condition and the described successive operations are applied again. If convergence is achieved the solution proceeds to the next time step. A thorough description of the technique as well as its implementation in *panMARE* is given in Gaschler (2017).

2.2 Structural Domain

As described in literature, see e.g. Wriggers (2008), the balance equations related to the solution of the structural domain can be written in the undeformed reference configuration as

$$\rho \ddot{\mathbf{d}} = \text{Div}(\mathbf{F}\mathbf{S}) + \rho \mathbf{b}. \quad (9)$$

Therein, $\ddot{\mathbf{d}}$ and $\dot{\mathbf{d}}$ denote the acceleration and velocity, respectively and \mathbf{d} is the unknown displacement field. $\mathbf{F} = \frac{\partial \mathbf{x}}{\partial \mathbf{X}}$ denotes the deformation gradient and \mathbf{S} is the second Piola-Kirchhoff stress tensor. The St. Venant-Kirchhoff model is employed to relate \mathbf{S} with the Green-Lagrange strain tensor

$$\mathbf{E} = \frac{1}{2}(\mathbf{F}^T \mathbf{F} - \mathbf{I}) \quad (10)$$

by

$$\mathbf{S} = \mathcal{C}\mathbf{E}. \quad (11)$$

Therein, \mathcal{C} corresponds to the elasticity tensor known from linear theory, where it describes the relation between the engineering strain and the Cauchy stress. Additionally, Dirichlet (displacement) and Neumann (traction) boundary conditions as well as homogeneous initial conditions are prescribed. In coupled simulations, the tractions are prescribed according to the results of the hydrodynamic domain. The structural subproblem is handled by the finite elements method (FEM) *AdhoC* and the structure in question is discretized spatially with high-order elements. The temporal discretization is carried out by means of the Newmark method.

2.3 Coupling

Having described the numerical treatment of fluid and structural domain, an FSI problem is formulated by introducing additional constraints. Obviously, the motion of the fluid boundary must follow that of the structure. This is achieved by prescribing the position of the panel corners of the fluid mesh. Utilizing Equation (6) and (7), structural deformations and the resulting velocities are considered in the hydrodynamic computation. For the structural domain, a Neumann type boundary condition is utilized to prescribe the occurring tractions on the structural side.

2.3.1 Coupling Algorithm

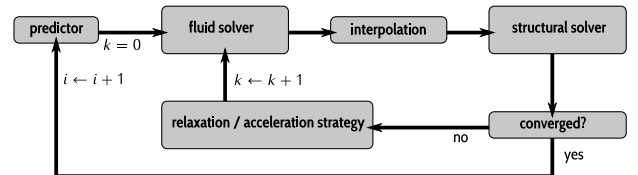


Figure 1: Coupling Algorithm.

Figure 1 presents a schematic depiction of the coupling algorithm. In this context, index i describes the time step

while index k refers to the current iteration. In each time step, a predictor provides an initial guess for the occurring deformations which are then applied to the BEM mesh. Having solved the hydrodynamic part of the problem, the resulting tractions are interpolated to the structural mesh. After solving the structural problem, the resulting deformations are checked for convergence against the last iterations' results. If no convergence is observed, another coupling iteration is initiated. In order to stabilize and accelerate the simulation, the Quasi-Newton Least-Squares method (Degroote et al., 2009) is employed. Therein, the Jacobian matrix of the deformation behaviour is approximated based on previous coupling iterations and a guess for the next iterations' deformation vector is given. Thus, the deformation field given by the structural solver is manipulated according to the Quasi-Newton Least-Squares method before it is applied to the fluid mesh. In this case, an interpolation is not needed to transfer information between the domains. The positions of the fluid nodes can be projected to the structural mesh and the ansatz functions of the respective structural element are then used to acquire the deformation at the point of interest. For a thorough description of the coupling algorithm's implementation, the reader is referred to Radtke et al. (2018).

2.4 Acoustic Domain

An acoustic evaluation of the simulations is performed in a post-processing fashion. Göttsche et al. (2017) present an overview of the technique, its implementation, as well as several validation cases, ranging from simple setups involving pulsating spheres to sophisticated simulations including a propeller in instationary inflow. Based on computed data regarding movement and loading of the bodies considered in the hydrodynamic domain, the FWHE in Formulation 1A (Brentner and Farassat, 2003) is employed. A distinction between contributions of fluid displacement p'_T and body loading p'_L is made to obtain the overall acoustic pressure p' ;

$$4\pi p'_T(\mathbf{x}, t) = \int_S \left[\frac{\rho(\dot{v}_n + v_{\dot{n}})}{\|\mathbf{r}\| (1 - M_r)^2} \right]_{\text{ret}} dS + \int_S \left[\frac{\rho v_n (\|\mathbf{r}\| \dot{M}_r + c M_r - c \|\mathbf{M}\|^2)}{\|\mathbf{r}\|^2 |1 - M_r|^3} \right]_{\text{ret}} dS \quad (12)$$

$$4\pi p'_L(\mathbf{x}, t) = \frac{1}{c} \int_S \left[\frac{\dot{l}_r}{\|\mathbf{r}\| (1 - M_r)^2} \right]_{\text{ret}} dS + \int_S \left[\frac{l_r - l_M}{\|\mathbf{r}\|^2 (1 - M_r)^2} \right]_{\text{ret}} dS + \frac{1}{c} \int_S \left[\frac{l_r (\|\mathbf{r}\| \dot{M}_r + c M_r - c \|\mathbf{M}\|^2)}{\|\mathbf{r}\|^2 |1 - M_r|^3} \right]_{\text{ret}} dS \quad (13)$$

$$p'(\mathbf{x}, t) = p'_T(\mathbf{x}, t) + p'_L(\mathbf{x}, t). \quad (14)$$

Equations (12) and (13) make use of the fluid density ρ , the surface velocity vector \mathbf{v} , the distance vector \mathbf{r} , which points from sound source point \mathbf{y} to the observer point \mathbf{x} , the surface velocity vector normalized by the speed of sound $\mathbf{M} = \frac{\mathbf{v}}{c}$, the speed of sound c and the pressure force vector $\mathbf{l} = p\mathbf{n}$. Here, \mathbf{n} refers to the surface unit normal vector. A dot over a variable marks a time derivative of that variable. The subscripts n , \dot{n} , r and M imply a dot product of that vector variable and the unit normal vector, the time derivative of the unit normal vector, the unit radiation vector, or the surface velocity vector normalized by the speed of sound, respectively. All values are taken at a retarded time

$$t_{\text{ret}} = t - \frac{\|\mathbf{r}\|}{c} \quad (15)$$

which refers to the time of emission.

3 SETUP

In this work, the SVA-P1356 propeller is investigated. Table 1 presents an overview of the setup. For simulations involving instationary inflow conditions, the wake field given in Figure 2 is used to describe the propeller inflow. In the following, simulations are conducted either at model or full scale, depending on the availability of experimental data. The ship wake is scaled accordingly while being considered as temporally invariant.

Table 1: P1356 propeller and environment.

Nr. of blades	n_B		5
Skew	s	[deg]	31.83
Diameter	$D(D_{MS})$	[m]	7.9 (0.25)
Fluid density	ρ	[kg m ⁻³]	1025.0
Speed of sound	c	[m s ⁻¹]	1500.0

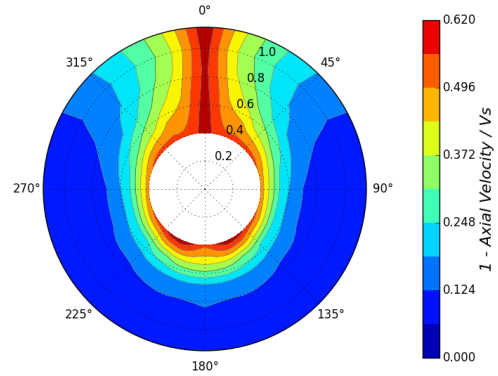


Figure 2: P1356 instationary inflow.

4 PRELIMINARY INVESTIGATIONS

In order to provide a sound computation of the coupled problems, naturally each participating domain needs to be solved properly. To this end, preliminary investigations were carried out, evaluating each field separately.

4.1 Fluid, stationary inflow

The hydrodynamic behaviour of the P1356 propeller in stationary inflow conditions is evaluated by means of *panMARE* simulation and the results are compared with those of experimental investigations (Richter and Heinke, 2006). An impression of the discretization of propeller blades and wake in the hydrodynamic calculations is given in Figure 3. In the

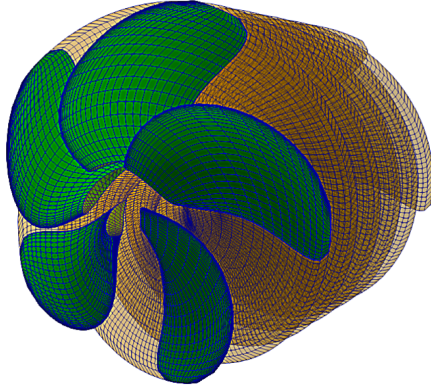


Figure 3: P1356 discretization for BEM.

resulting open water diagram, see Figure 4, it can be seen that the behaviour of the thrust coefficient was captured very well while there are considerable differences with regard to the torque coefficient, especially at low advance coefficients. As the thrust is expected to be the dominating influence on the blade deformations, the results are quite promising with regard to coupled simulations.

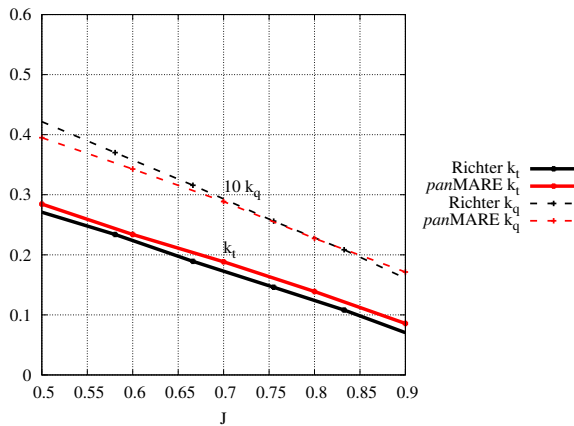


Figure 4: P1356 Open Water Diagram.

4.1.1 Cavitation

As cavitation is expected to have a large effect on the acoustic signature of the propeller as well as its overall performance, a brief investigation of the cavitation model used here is conducted and the cavitation area as well as the measured thrust, torque and efficiency are compared with experiments (Richter and Heinke, 2006). Details of the computed setup are given in Table 2. Figure 5 gives an impression of the occurring cavitation effects. In general, the cavity shape was captured very well. As no tip vortex

Table 2: P1356 stationary inflow and cavitation. Model scale.

Advance coefficient	J	0.6
Rotation rate	n [s ⁻¹]	25
Cavitation number	σ_n	2.312

model was used, such phenomena are not captured. Toward the trailing edge of the blade, no cavitation is present in the simulations although in the experiments a continuous cavity extending from leading edge to trailing edge was observed. The resulting values for thrust and torque

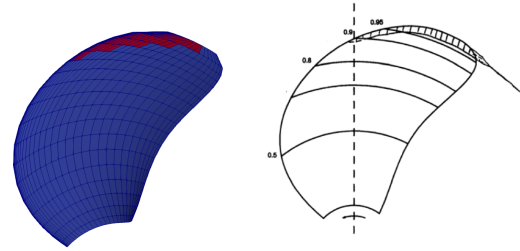


Figure 5: P1356 cavitation in stationary inflow.

coefficient are given in the bar chart presented in Figure 6. Although a quantitative assessment of the results yields considerable differences, the qualitative behaviour of both thrust and torque could be captured in the simulations. The slight increase in thrust and torque in the cavitating case is attributed to an increase of blade thickness due to the cavity.

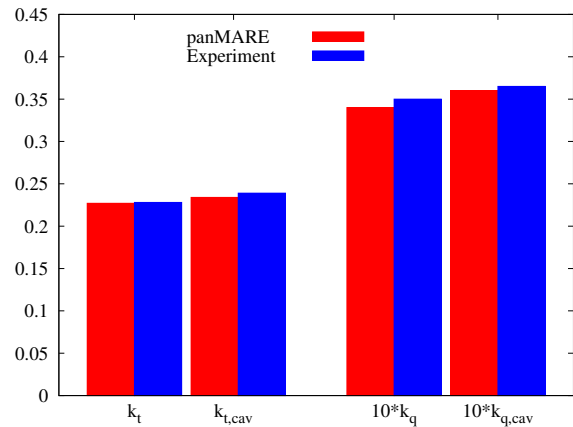


Figure 6: P1356 cavitating thrust and torque. Stationary inflow. Advance coefficient $J = 0.6$

4.1.2 Instationary cavitation

In addition to the previous investigations, the P1356 propeller is simulated for instationary inflow conditions, see Figure 2. In this case, the inflow velocity is prescribed such that the mean thrust coefficient measured in the corresponding experiments (Heinke and Jaksic, 2003) is also present in the simulations. Table 3 summarizes the simulation parameters. Figure 7 gives an optical impression

Table 3: P1356 instationary inflow and cavitation. Model scale.

Cavitation number	σ_n	1.489
Rotation rate	n [s ⁻¹]	30
Mean thrust coefficient	$k_{t,m}$	0.172

of the computed cavity shape as well as the experimental results at a blade rotation angle of $\theta = 20^\circ$. Similar to the observations regarding cavitation in stationary inflow, the general shape of the cavity was captured quite well. Again, the behaviour towards the blade tip trailing edge differs between experiments and simulation as no tip vortex model is employed.

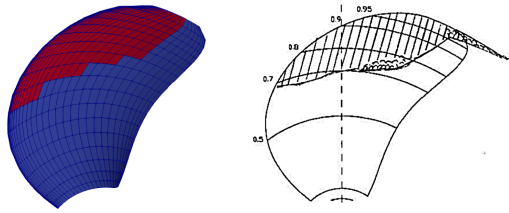


Figure 7: P1356 cavitation in instationary inflow. Rotation angle $\theta = 20^\circ$.

4.2 Structure

In order to ascertain a correct structural modelling of the propeller blades, the convergence behaviour of the structural mesh is investigated. A static test case is considered, in which a large deformation of the propeller blade is enforced by prescribing a volume load. Exemplary pictures of the utilized discretizations are given in Figure 8. Figure 9

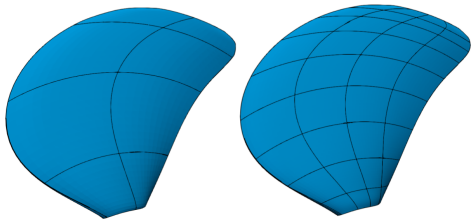


Figure 8: Exemplary structural meshes.

shows the convergence of the mean relative error in the computed strain energy $\| \frac{E - E_{ref}}{E_{ref}} \|$ for different refinement strategies. The reference solution is obtained using a highly refined mesh. The expected superior convergence behavior of the p -FEM over classical h -FEM can clearly be observed. Special consideration must be given to the combination of element order p and geometric order p_g as only iso- or subparametric formulations yield reliable results.

5 COUPLED SIMULATIONS

Since the preliminary investigations provided sufficient confidence in the modelling of structural as well as fluid domain, coupled simulations are carried out in the following.

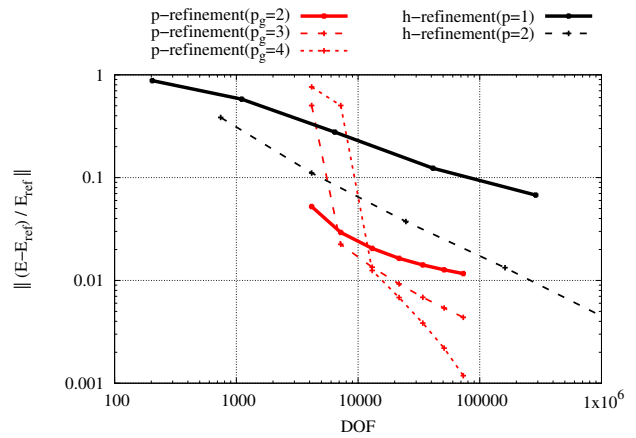


Figure 9: Structural Mesh Convergence.

Firstly, a setup involving homogeneous inflow conditions as well as cavitation effects is computed. In the next step, the flexible propeller is calculated in inhomogeneous inflow conditions and the resulting tip deformation as well as blade thrust coefficient progression is analysed. In order to assess the capabilities of the method regarding the influence of FSI on the acoustic signature, another setup is computed in which the propeller is excited by a time-varying volume load and the resulting acoustic spectrum is evaluated.

5.1 Setup 1

The first setup corresponds to the simulation parameters given in Table 2. The propeller is simulated at model scale. The material parameters used here are given in Table 4. In this case a very soft material was used to highlight the capabilities of the method with regard to the simulation of large deformations and their influence on propeller performance and cavitation. Obviously, the used material properties would not actually be used to build a propeller but are rather meant to showcase the simulation method presented here. The results are summarized in Figure 10. Due to

Table 4: P1356 stationary inflow and cavitation. Material parameters.

Poisson ratio	ν	0.41
Young's modulus	E [Nm ⁻²]	$2.5 \cdot 10^8$
Density	ρ [kgm ⁻³]	1180

the deformation of the blade, thrust as well as torque coefficient are reduced. As expected, the propeller efficiency is reduced, too. Due to the deformation and the induced reduction of the loads on the blade, cavitation is not present on the blade anymore. The decrease in thrust and torque experienced by the propeller reflects in the observed deformation field. Figure 11 presents the deformation of the blade median plane along the propeller shaft axis at different relative radii over the respective chord length. Due to the selected material, the maximum deformation amounts to almost 10 % of the propeller diameter. Since leading and trailing edge are deformed differently, the blade pitch angle changes. The change in pitch angle, estimated by

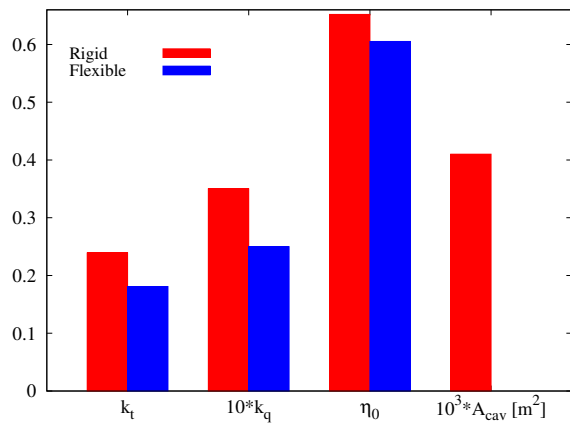


Figure 10: P1356 in stationary inflow. Results from rigid and flexible simulation.

means of the deformation at leading and trailing edge and the assumption of an invariant chord length, is also given in Figure 11 via the annotations associated with the respective section cuts.

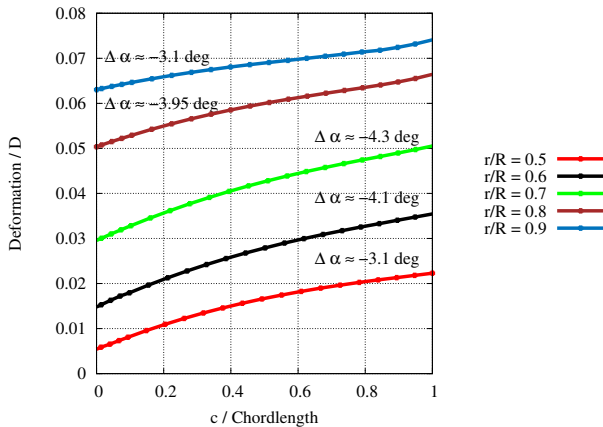


Figure 11: P1356 deformation field in stationary inflow.

5.2 Setup 2

The second configuration that is investigated is the P1356 propeller in instationary inflow conditions. Figure 2 shows the prescribed inflow field while the simulation parameters are given in Table 3. Again, the propeller is calculated at model scale. Here, an increased Young's modulus of $E = 12.5 \cdot 10^8$ Pa was used in order to ensure the stability of the simulation. The behaviour of the thrust coefficient associated with one of the propeller's blades over the course of one propeller rotation is displayed in Figure 12. Due to the consideration of the FSI, an unsteady behaviour is observed with respect to the blade loads which originates in the changing deformation field of the blade. In addition, the progression of the thrust coefficient is altered such that after the blade leaves the vicinity of low inflow velocities in the 12 o'clock position of the wake field, the drop in thrust coefficient is not as pronounced as for the rigid case. The behaviour of the blade thrust coefficient is reflected in the

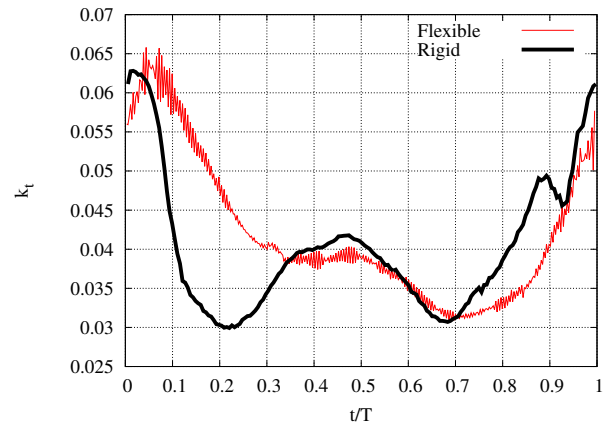


Figure 12: P1356 blade k_t in instationary inflow.

occurring deformations. Figure 13 shows the deformation in direction of the propeller shaft axis of a point located near the midchord position of the propeller tip. It can be

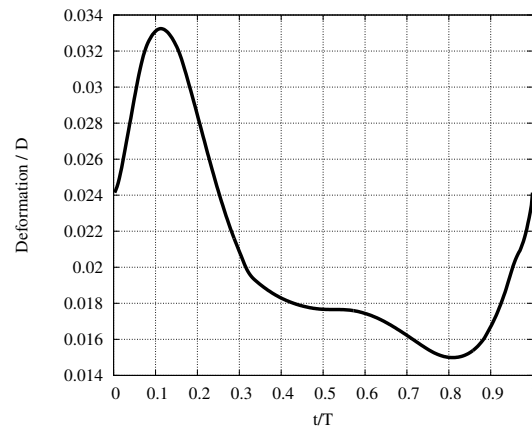


Figure 13: P1356 blade tip deformation in instationary inflow.

observed that the tip deformation resembles the progression of the thrust coefficient. Similar to the observations made in Section 5.1, leading and trailing edge experience different deformations though, thus changing the pitch angle, which is assumed as the dominant effect responsible for the altered performance of the propeller.

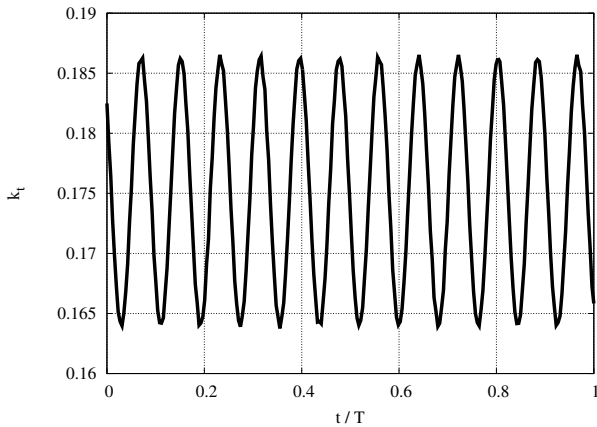
5.3 Setup 3

In this setup, the P1356 propeller is again simulated in homogeneous inflow conditions. The blade is excited by a sinusoidally varying volume load and the influence of the occurring deformations on performance and acoustic signature is evaluated. The volume load acts parallel to the propeller shaft axis. Noise induced by the propeller is evaluated at an observation point located 100 m in front of the propeller. The simulations were conducted at full scale in order to ease the requirements on the time step size, which largely depend on the rotation rate and blade Eigenfrequency. Table 5 summarizes the simulation parameters as well as material properties. Due to the prescribed excita-

Table 5: P1356 stationary inflow. Full Scale.

Advance coefficient	J	0.75
Rotation rate	n [s ⁻¹]	2.5
Density	ρ [kgm ⁻³]	8150
Poisson ratio	ν	0.3
Young's modulus	E [Nm ⁻²]	$2.0 \cdot 10^{11}$
Excitation frequency	ω [s ⁻¹]	36

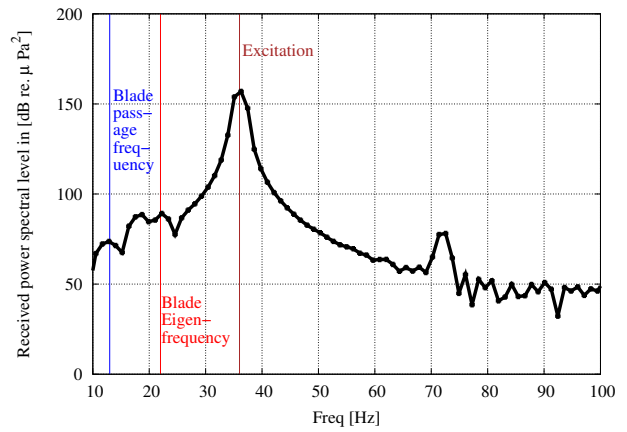
tion, the 1st bending mode of the blade is excited primarily and the blade enters a back and forth bending motion with an amplitude of about 20 mm. The influence of the excitation on the blade loads is shown in Figure 14 which presents the thrust coefficient over one rotation period. In accor-

**Figure 14:** P1356 k_t in stationary inflow. Excitation by volume load.

dance with the blade motion induced by the FSI effects, the thrust coefficient displays a sinusoidal behaviour with a mean of $k_t = 0.175$. The propeller experiences, compared to the behaviour of a rigid propeller, an increased thrust coefficient. As an opposite effect was observed in Section 5.1, the amount of flexibility seems to dictate the qualitative influence on the propeller loads. This effect should be subject of further investigations. Due to to described behaviour of blade motion and loading, the respective terms in Equation (14) are affected and the prescribed excitation heavily influences the acoustic spectrum at the observation point. A plot of the computed sound pressure levels (SPL) against frequencies is given in Figure 15. The most dominating frequency is attributed to the excitation. Smaller peaks in the spectrum are observed at the structural blade Eigenfrequency as well as the blade passage frequency.

6 CONCLUSION

A partitioned solution approach with regard to fluid-structure interaction problems arising from the modelling of the dynamic behaviour of flexible marine propellers was presented. Therein, the fluid domain is simulated by means of a potential theory based boundary element method with an additional model to take into account sheet cavitation. The structural part of the problem is handled by a high-order finite elements method. Information exchange be-

**Figure 15:** P1356 sound pressure levels. Excitation by volume load.

tween the respective sub-problems is managed by a separate coupling tool which employs the Quasi-Newton Least-Squares method to provide a stable and efficient computation method. Acoustic evaluation is performed in a post-processing fashion using the Ffowcs-Williams Hawkins equation. In the following, the P1356 propeller is investigated. Preliminary investigations regarding the hydrodynamic and structural domain are carried out. A comparison of the hydrodynamic characteristics of the (cavitating) propeller in stationary and instationary inflow conditions against experimental data shows promising results. On the structural side, an appropriate convergence behaviour of the model is ensured.

Conclusively, coupled simulations of the propeller were carried out. Considering the structural deformations in the hydrodynamic computations leads to a physically consistent behaviour regarding the influence on propeller performance and its acoustic signature. Future research and development consider a validation of the partitioned solution approach, as well as the acoustic evaluation of simulation cases which are, regarding material properties and operation state, more closely related to actually operating propellers.

ACKNOWLEDGEMENT

The authors gratefully acknowledge the support provided by the DFG (German Science Foundation – Deutsche Forschungsgesellschaft) under the grant numbers AB 112/12-1 and DU 405/13-1. Special thanks is also given to the SVA for providing the experimental measurements.

REFERENCES

- Berger, S. , Druckenbrod, M. , Pergande, M. , and Abdel-Maksoud, M. . A two-stage optimization method for full-scale marine propellers working behind a ship. *Ship Technology Research*, 61:64–79, 2014.
- Brentner, K. and Farassat, F. . Modeling aeodynamically generated sound of helicopter rotors. *Progress in Aerospace Sciences*, 2003. doi: doi:10.1016/S0376-0421(02)00068-4.

- Degroote, J. , Bathe, K. , and Vierendeels, J. . Performance of a new partitioned procedure versus a monolithic procedure in fluid-structure interaction. Computers & Structures, 87(11):793 – 801, 2009.
- Düster, A. , Bröker, H. , and Rank, E. . The p-version of the finite element method for three-dimensional curved thin walled structures. International Journal for Numerical Methods in Engineering, 52:673–703, 2001.
- Gaschler, M. . Numerical Modelling and Simulation of Cavitating Marine Propeller Flows. PhD thesis, Technical University of Hamburg, 2017.
- Göttsche, U. , Scharf, M. , Berger, S. , and Abdel-Maksoud, M. . A Hybrid Numerical Method for Investigating Underwater Sound Propagation of Cavitating Propellers. In Proceedings of the Fifth International Symposium on Marine Propulsors - smp'17, 2017.
- Heinke, H. and Jaksic, D. . Untersuchung des Einflusses des Nachstromfeldes (Modell- oder Großausführungsnachstrom) auf die Kavitation und Druckschwankungen am KRISO Containerschiff KS621. Technical report, Schiffbau-Versuchsanstalt Potsdam GmbH, 2003.
- König, M. , Radtke, L. , and Düster, A. . A flexible C++ framework for the partitioned solution of strongly coupled multifield problems. Computers & Mathematics with Applications, 72(7):1764–1789, 2016.
- Neitzel, J. , Pergande, M. , Berger, S. , and Abdel-Maksoud, M. . Influence of the numerical propulsion modelling on the velocity distribution behind the propulsion device and manoeuvring forces. In Fourth International Symposium on Marine Propulsors, 2015.
- Radtke, L. , Lampe, T. , Abdel-Maksoud, M. , and Düster, A. . A partitioned solution approach for the simulation of the dynamic behaviour of flexible marine propellers. Ship Technology Research, 2018. doi: 10.1080/09377255.2018.1542782.
- Richter, H. and Heinke, H.-J. . Freifahrt- und Kavitationsversuche sowie Druckschwankungsmessungen mit dem Propeller P1356 in homogener Zuströmung. Technical report, Schiffbau-Versuchsanstalt Potsdam GmbH, 2006.
- Wriggers, P. . Nonlinear Finite-Element-Methods. Springer-Verlag, 2008.